Bull. Mater. Sci., Vol. 40, No. 6, October 2017, pp. 1137–1149
DOI 10.1007/s12034-017-1470-5

Facile synthesis and characterization of rough surface V_2O_5 nanomaterials for pseudo-supercapacitor electrode material with high capacitance

YIFU ZHANG* and **YUTING HUANG**
School of Chemistry, Dalian University of Technology, Dalian 116024, People's Republic of China
*Author for correspondence (yfzhang@dlut.edu.cn)

MS received 27 June 2016; accepted 12 February 2017; published online 20 September 2017

Abstract. V_2O_5 nanomaterials with rough surface were synthesized using commercial V_2O_5, ethanol (EtOH) and H_2O as the starting materials by a simple hydrothermal route and combination of calcination. The electrochemical properties of V_2O_5 nanomaterials as electrodes in a supercapacitor device were measured using cyclic voltammetry (CV) and galvanostatic charge–discharge (GCD) method. V_2O_5 nanomaterials exhibit the specific capacitance of 423 F g^{-1} at the current density of 0.5 A g^{-1} and retain 327 F g^{-1} even at the high current density of 10 A g^{-1}. The influence of the ratio of EtOH/H_2O, the calcined time and temperature on the morphology, purity and electrochemical property of the products is discussed in detail. The results revealed that the ratio of EtOH/H_2O = 10/25 and calcination at 400°C for 2–4 h are favourable for preparing V_2O_5 nanomaterials and they exhibited the best electrochemical property. The novel morphology and high specific surface area are the main factors that contribute to high electrochemical performance of V_2O_5 nanomaterials during the charge–discharge processes. It turns out that V_2O_5 nanomaterials with rough surface is an ideal material for supercapacitor electrode in the present work.

Keywords. V_2O_5; nanomaterials; electrical properties; supercapacitor.

1. Introduction

In the recent past, lot of attention has been paid to the field of alternative energy storage/conversion devices with high power and energy densities owing to the tremendous demands for digital communications, electronic devices, mobile phones, renewable energy vehicles, etc. [1–8]. Among various energy storage devices, supercapacitors, also called ultracapacitors or electrochemical capacitors, have drawn great interest because of their superiorities of excellent power output, superior rate capability, exceptional cycling life, lightweight and ease of handing [4,9,10], and these unique properties make them available as power sources for the next-generation flexible and portable electronics such as roll-up displays, miniature biomedical devices and wearable devices [9]. Generally, supercapacitors are classified into two types according to their storage mechanism: the electrochemical double-layer capacitors (EDLCs) (non-Faradic process) and pseudocapacitors (Faradic redox process). EDLCs physically store charges by reversible ion adsorption at the electrode–electrolyte interface, while pseudocapacitors chemically store their charges by redox reaction at the vicinity (a few nanometres) of the surface [1,11]. Typically, electrode materials for EDLCs are composed of high-surface-area carbon-based materials, while those for pseudocapacitors are conductive polymers and transition metal oxides/hydroxides/sulphides [12]. Electrochemical capacitors based on transition metal oxides/hydroxides/sulphides exhibit much higher specific capacitance than conventional carbon materials and better electrochemical stability than conducting polymers [13–16]. However, the energy density (E) of conventional supercapacitors is commonly less than 10 W h kg^{-1}, which is much lower than those of batteries and fuel cells, hampering their practical applications [2]. As is well known, the energy density of a supercapacitor is governed by the capacitance (C) and voltage (V), according to the equation $E = (1/2)CV^2$. Thus, increasing the device capacitance with novel electrode materials becomes an efficient strategy to improve the energy density of supercapacitors [17].

Over the past decades, enormous attention has been paid to transition metal oxides/hydroxides/sulphides electrode materials. Among the various metal oxides, vanadium oxides (VO_x) have received increasing interest as supercapacitor electrodes because of their low cost, multiple valence states (V^{5+}, V^{4+}, V^{3+} and V^{2+}) and unique layered structure, which play a major role in delivering high energy

Electronic supplementary material: The online version of this article (doi:10.1007/s12034-017-1470-5) contains supplementary material, which is available to authorized users.

density and allowing efficient ion diffusion [10,15,17–30]. VO_x with novel structures have better capacitive property than massive VO_x due to the charge storage mechanism, and the electrochemical performance of energy storage elements is closely related to the morphology and crystal structure of electrode materials [31,32]. The contact area between the electrode materials and electrolyte can be significantly increased by controlling the morphology of electrode materials. Meanwhile, the distance that the ions have to transit in the electrolyte is shortened greatly [1]. As a result, the electrochemical properties can also be improved. As the family of VO_x, vanadium pentoxide (V_2O_5) is considered to be one of the most promising candidates [31,33–36]. Therefore, in the recent years, nano-structured V_2O_5 with different morphologies, including hollow spheres [17], microspheres [11], thin films [37], nanofibres [15], nanowires [38], nanoribbons [39], nanotubes [40], nanorods [32], nanoporous structures [41], nanosheets forming 3D architectures [31], interconnected V_2O_5 nanoporous network [34], etc. have been synthesized by different approaches and their activity tested for supercapacitor applications. For example, V_2O_5 nanoflowers, nanoballs, nanowires and nanorods were synthesized through a simple hydrothermal method reported by Mu *et al* [32] and they exhibited specific capacitance, respectively, of 119, 161, 177 and 235 F g^{-1} at the current density of 1 A g^{-1}. Wee *et al* [15] prepared electrospun V_2O_5 nanofibres by the electrospinning method and obtained high capacitance of 304 F g^{-1}. Ultrahigh-aspect-ratio V_2O_5 nanowires were prepared by a template-free hydrothermal route and it exhibited a high capacitance of 351 F g^{-1} at the current density of 1 A g^{-1}, as reported by Wang *et al* [38]. Saravanakumar *et al* [34] synthesized an interconnected V_2O_5 nanoporous network using sodium citrate as a capping agent by a simple capping-agent-assisted precipitation technique. It showed the specific capacitance of 304 F g^{-1} at a current density of 0.1 A g^{-1} by the galvanostatic charge–discharge (GCD) method. Yang *et al* [17] reported that hollow V_2O_5 microspheres were fabricated by a solvothermal approach and it exhibited the maximum capacitance of 479 F g^{-1}. Our previous work reported that V_2O_5 nanobelts, nanoparticles and microspheres were synthesized by a simple hydrothermal route and combination of calcination and they displayed specific capacitance, respectively, of 140, 276 and 308 F g^{-1} at the current density of 1 A g^{-1} [11]. These synthesis methods clearly demonstrate that V_2O_5 nanostructures have significant effect on their pseudocapacitance behaviour. Generally, the performance of electrochemical supercapacitors of V_2O_5 materials can be achieved in two strategies. The first one is encapsulating V_2O_5 with carbonaceous materials, such as amorphous carbon [42], carbon nanotubes [43], graphene [19] and so on. The second strategy is to synthesize V_2O_5 nanomaterials with novel structures because nanostructured materials provide high surface area and short diffusion paths, which can provide more electrochemically active sites and increase the contact area between the electrode and electrolyte during the electrochemical reactions [1]. Therefore, to synthesize V_2O_5 with novel structures to improve the specific capacitance of V_2O_5 electrodes is still a challenge and meaningful for materials scientists.

In this work, we developed a facile route to successfully synthesize V_2O_5 nanomaterials with rough surface using commercial V_2O_5, ethanol (EtOH) and H_2O as the starting materials by a simple hydrothermal method and combination of calcination. Their electrochemical properties by cyclic voltammetry (CV) and GCD as pseudo-supercapacitor electrode material are discussed in detail.

2. Materials and methods

2.1 *Materials*

Commercial vanadium pentoxide (V_2O_5), and absolute ethanol (CH_3CH_2OH , EtOH) of analytical grade were purchased from Sinopharm Chemical Reagent Co., Ltd, and used without any further purification.

2.2 *Methods*

To transform commercial V_2O_5 powder into V_2O_5 nanomaterials, the experimental procedure included two steps: (1) 0.91 g of V_2O_5 powder was dispersed into the mixed solution (the total volume of deionized water and ethanol was 35 ml and the volume ratio of ethanol/water (EtOH/H_2O) was 0/35, 2/33, 5/30, 10/25, 15/20 and 25/10) with vigorous stirring for 1 h at room temperature. After the solutions became suspensions, they were transferred into a 50 ml teflon-lined stainless-steel autoclave, which was sealed and maintained at 180°C for 48 h and then naturally cooled to room temperature. After the reaction, the products were filtered off, washed with distilled water and absolute ethanol several times to remove any possible residues and dried in vacuum at 75°C. (2) The above products were heated in a muffle furnace at 5°C min^{-1} heating rate in air atmosphere at 300−500°C for 2–12 h, and cooled to room temperature naturally.

2.3 *Materials characterization*

The phase and composition of the products were identified by powder X-ray diffraction (XRD, Panalytical X'Pert powder diffractometer at 40 kV and 40 mA with Ni-filtered Cu $K\alpha$ radiation). Fourier transform infrared spectroscopy (FTIR) pattern of the solid samples was obtained by the KBr pellet technique (about 1 wt% of the samples and 99 wt% of KBr were mixed homogeneously, and then the mixture was pressed to a pellet) and recorded on a Nicolet 6700 spectrometer from 4000 to 400 cm^{-1} with a resolution of 4 cm^{-1}. The morphology and dimensions of the products were observed by field emission scanning electron microscopy (FE-SEM, NOVA NanoSEM 450, FEI) and transmission electron microscopy (TEM, FEITecnai F30, FEI). The samples were dispersed in absolute ethanol with ultrasonication before TEM characterization. Surface area was determined by the

Brunauer–Emmet–Teller (BET) method using a Micromeritics ASAP-2020 system and the samples were degassed at 150°C for several hours.

2.4 *Electrochemical characterization*

Electrochemical tests were performed using a three-electrode cell, in which Ni-grid and saturated calomel electrode (SCE) were used as the counter and the reference electrode, respectively. The working electrodes were comprised of 80 wt% of active material (V_2O_5 nanomaterials), 10 wt% of carbon black and 10 wt% of polyvinylidene difluoride (PVDF). N-methyl-2-pyrrolidone (NMP) was used as a solvent. The mixed slurries were coated onto Ni foils and heated at 80°C overnight to remove the organic solvent. Then these foils were pressed onto Ni-grids at a pressure of 10 MPa. The electrolyte was 1 mol l^{-1} $LiNO_3$ solution. Cyclic voltammetry (CV), GCD and electrochemical impedance spectroscopy (EIS) were used to investigate the electrochemical performance of the electrode materials. CV data were collected between −0.6 and 0.8 V at different scan rates (5–100 mV s^{-1}) and GCD tests were performed in the potential range of −0.6 to 0.8 V at a current density of 0.2–20 A g^{-1}.

The specific capacitance (C, F g^{-1}) and energy density (E, W h kg^{-1}) of the active material in the electrode, determined using charge–discharge curves, can be calculated from the following equations:

$$C = \frac{I \cdot \Delta t}{m \cdot \Delta V} \tag{1}$$

$$E = \frac{1}{2} C (\Delta V)^2, \tag{2}$$

where C (F g^{-1}) is the specific capacitance, I (A) is the discharge current, Δt (s) is the discharge time, m (g) is the mass of the active material in the working electrode, ΔV (V) represents the potential drop during the discharge process and E (W h kg^{-1}) is the energy density. The power density P (W kg^{-1}) can be calculated from the energy density E and the discharge time Δt according to the following equation:

$$P = \frac{E}{\Delta t}. \tag{3}$$

3. Results and discussion

3.1 *Physical characterization of the product V_2O_5 nanomaterials*

Figure 1 shows the typical XRD of the product synthesized at $EtOH/H_2O = 10/25$ and calcination at 400°C for 4 h. All the diffraction peaks from figure 1b can be indexed as the orthorhombic crystalline phase of V_2O_5 (space group: Pmmn 59) with lattice constants values of $a = 11.516$ Å, $b = 3.5656$ Å and $c = 4.372$ Å (JCPDS, Number 41-1426), whose plots are depicted in figure 1a. No obvious peaks of any other impurities, such as V_6O_{13}, V_3O_7, VO_2 and V_2O_3, are detected, revealing that the synthesized V_2O_5 material has a high purity.

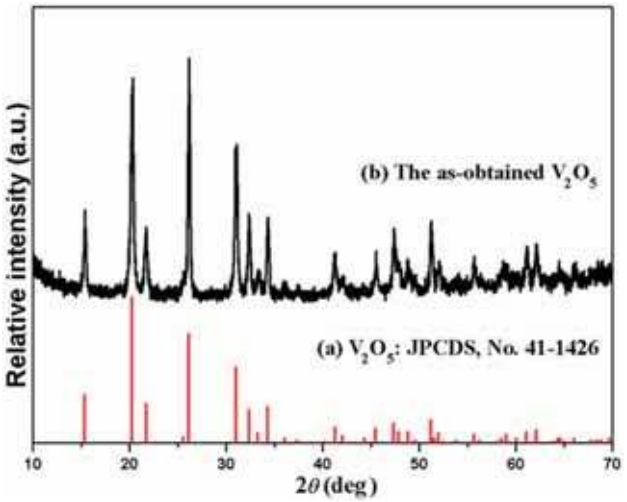

Figure 1. XRD patterns of the as-obtained V_2O_5.

The morphology and size of this product were measured by FE-SEM and TEM, as shown, respectively, in figures 2 and 3. FE-SEM images (figure 2) show that the as-synthesized product consists of a large number of one-dimensional (1D) nanostructures with length up to several micrometres. High-magnification FE-SEM images (figure 2c and d) reveal that the as-obtained V_2O_5 nanostructures have rough surface and we can also observe their thickness, suggesting that the morphology of the as-synthesized V_2O_5 is mainly belt-like shape. Further morphology information of V_2O_5 nanomaterials is provided by TEM. The TEM images (figure 3a–c) also show that V_2O_5 nanomaterials with belt-like shape are observed and their surface is very rough, which agrees with the FE-SEM observations well. The prepared V_2O_5 nanomaterials have rough surface due to the calcining process of transforming low vanadium oxides to V_2O_5 in agreement with the previous report [21], which suggests that these V_2O_5 nanomaterials have high supercapacitor capacitance [44]. The high-resolution TEM (HRTEM) image (figure 3d) of the as-prepared V_2O_5 nanomaterials shows that the distance between the neighbouring planes is 2.75 Å, which is in agreement with the (001) plane of orthorhombic V_2O_5 in the XRD patterns (figure 1). The HRTEM image also reveals that the as-prepared V_2O_5 nanomaterials are crystallized without the presence of dislocations and defects. Supplementary figure S1 shows the FE-SEM images of the commercial V_2O_5 and reveals that the morphology of the commercial V_2O_5 is irregular with large particles. Thus, bulk V_2O_5 can be easily transformed to V_2O_5 nanomaterials with rough surface by this hydrothermal route and combination of calcination.

Figure 4a depicts the FTIR spectrum of the as-prepared V_2O_5 nanomaterials. The absorption peaks ranging from

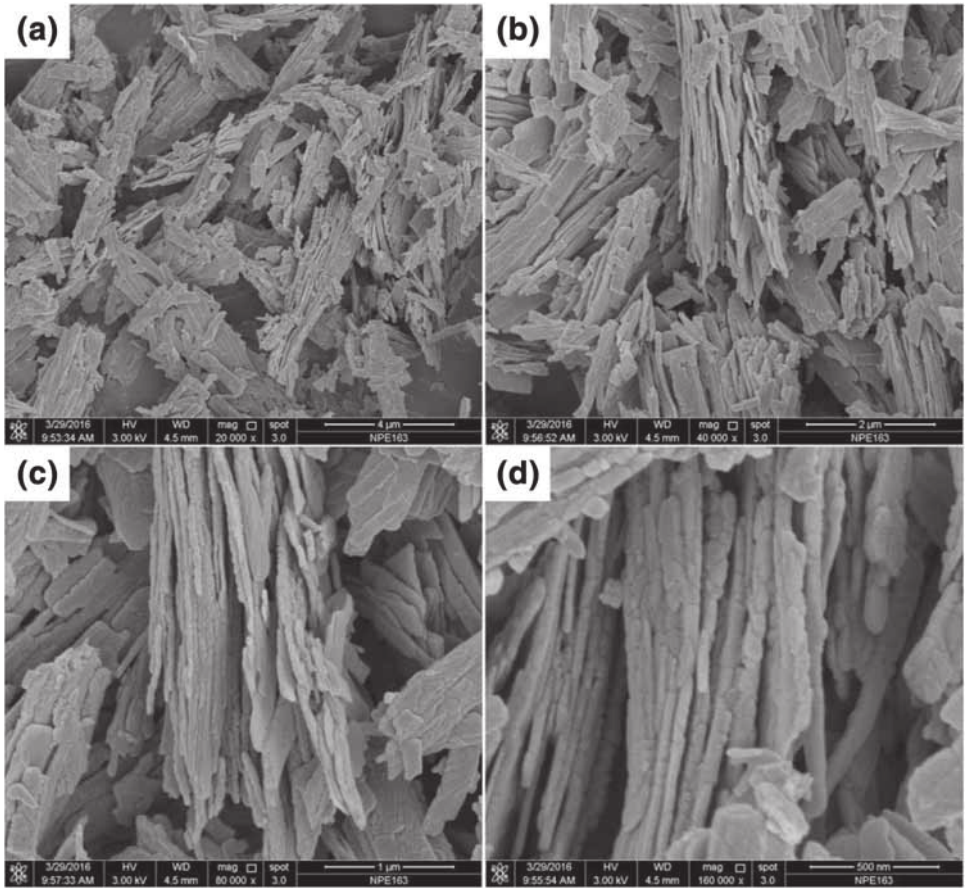

Figure 2. FE-SEM images of the as-obtained V_2O_5.

1200 to 400 cm^{-1} are assigned to the characteristic of V–O vibration band [11,21,45]. The absorption peak at 1023 cm^{-1} is attributed to the symmetric stretching vibration of $V^{5+} = O$ bond, which is the characteristic structure of the layered orthorhombic V_2O_5 [46]. The absorption band at 834 cm^{-1} is indexed to the vibration of $O-(V)_3$ [47]. The absorption peaks at 615 and 476 cm^{-1} correspond, respectively, to the asymmetric and the symmetric stretching modes of V–O–V bridging bonds. In addition, the absorption peaks at 3430, 2363 and 1632 cm^{-1} are attributed to the stretching modes of water and carbon dioxide molecules adsorbed on the samples and can be disregarded. Figure 4b shows the Raman spectrum of the as-prepared V_2O_5 nanomaterials, which reveals that the V_2O_5 nanomaterials have prominent Raman vibrational frequencies in the range of 50–1100 cm^{-1} and these vibrational modes are characteristic of orthorhombic V_2O_5 [48–52]. The bands at 94, 138, 191 and 299 cm^{-1} are ascribed, respectively, to A_g, B_{3g}, A_g and A_g modes owing to the stretching vibration mode of $(V_2O_2)_n$ that corresponds to the chain translation. The detection is strongly associated with $[VO_5]$ units in layered structure (the oxide-layered structure). Particularly, the band at 138 cm^{-1} is very sharp, strong and dominant, indicating that the crystalline V_2O_5 has a very-long-range order [53]. Two peaks observed at 2851 (B_{2g} mode) and 405 cm^{-1} (A_g mode) are, respectively, indexed to the bending vibration of the $O_3-V=O$ and $V-O_3-V$ bonds. The band at 471 cm^{-1} (A_g mode) is assigned to the bending vibration of the bridging $V-O_2-V$ (doubly coordinated oxygen). The vibrational band located at 523 cm^{-1} (A_g mode) is assigned to the triply coordinated oxygen (V_3-O) stretching mode. The band at 688 cm^{-1} (B_{2g} mode) corresponds to the doubly coordinated oxygen (V_2-O) stretching mode. The peak at 991 cm^{-1} (A_g mode) is indexed to the stretching vibration mode of the double bond (V=O) involving the terminal unshared O oxygen. The results of FTIR and Raman analyses are in accordance with the result of XRD analysis.

Figure 5 shows the N_2 adsorption–desorption isotherms of the as-prepared V_2O_5 nanomaterials and the commercial V_2O_5. The isotherms show a sharp capillary condensation step at high relative pressure and belong to type IV isotherm according to IUPAC classification. The BET results clearly show that the specific surface area of the V_2O_5 nanomaterials is 10.1 $m^2\ g^{-1}$, which is larger than the value of the commercial V_2O_5 (4.9 $m^2\ g^{-1}$). However, this value is lower than the value (45.6 $m^2\ g^{-1}$) reported by Rui *et al* [6], and their high value may be owing to their novel synthesis method.

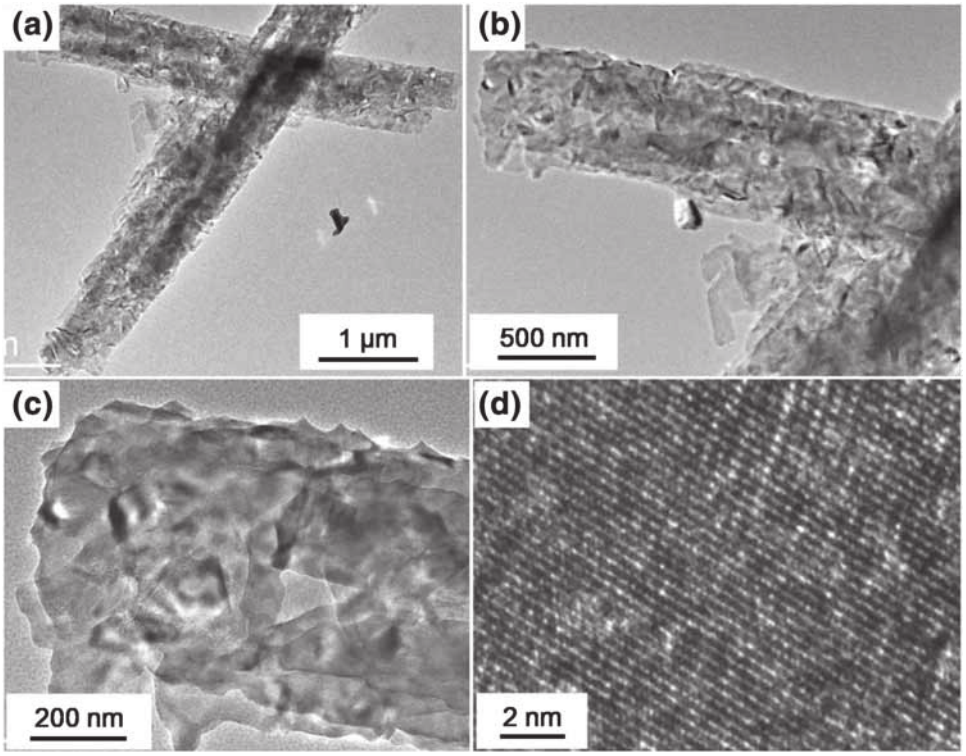

Figure 3. TEM images of the as-obtained V_2O_5.

3.2 *Influence of synthesis conditions on the phase and morphology of the products*

Like other low dimensional nanomaterials of vanadium oxides [21,54], specific conditions are required to prepare V_2O_5 nanomaterials. It was found from a series of experiments that the ratio of the EtOH/H_2O, the calcined time and temperature had significant effects on the morphology and purity of the final products. The volume ratio of EtOH/H_2O plays a crucial role in preparing V_2O_5 nanomaterials. Keeping other parameters constant, only the volume ratio of EtOH/$H_2O$was considered as the changeable parameter. The synthesis reactions were carried out with different volume ratios of EtOH/H_2O = 0/35, 2/33, 5/30, 10/25, 15/20, 25/10 and calcination at 400°C for 4 h. The synthesized products were separately characterized by XRD and FE-SEM, as shown in figures 6 and 7, respectively. When the ratio of EtOH/$H_2O$was 0/35, pure-phase V_2O_5 with irregular particles was prepared, as depicted in figures 6b and 7a. With the increase of the ratio of EtOH/H_2O to 2/33 (figure 6c) and 5/30 (figure 6d), the phases V_2O_5 were also obtained; however, an impure peak at 33.7° was observed, which was the diffraction peak of V_4O_9 from the calcination of low-valence vanadium oxide hydrate $V_3O_7 \cdot H_2O$ [55]. This peak gradually weakened and even disappeared with the increase of the ratio of EtOH/H_2O, as shown in figure 6c–e. Their morphologies mainly consisted of nanoparticles and fragments (figure 7b and c); nevertheless, belt-like shapes were also observed, indicating that belt-like morphology was formed with the increase of the ratio of EtOH/H_2O. When the ratio of EtOH/H_2O was continuously increased (figure 6e–g), pure-phase V_2O_5 was obtained. V_2O_5 nanomaterials with belt-like shapes were synthesized at the ratio of EtOH/H_2O = 10/25 (figures 2 and 3); however, the nanobelts became short and some particles were seen as shown in figure 7d. Therefore, these analyses reveal that the ratio of EtOH/H_2O is a critical factor for synthesizing vanadium oxides nanostructures and the ratio of EtOH/H_2O = 10/25 is favourable for preparing V_2O_5 nanomaterials.

The calcination temperatures and times also play an important role in controlling the phases and morphologies of the final products, as depicted in figures 8 and 9. Comparative experiments were carried out by varying the calcination temperature at 300−500°C, while keeping other synthesis parameters constant (EtOH/H_2O= 10/25 and calcination time = 4 h). When the calcination temperature was 300°C for 12 h, VO_2 (JCPDS, Number 65-7960) was obtained (figure 8b). When the temperature was increased to 400−500°C, pure-phase V_2O_5 was prepared. However, the morphology of V_2O_5 obtained at 500°C became irregular, as seen by comparing figures 9c and 2. Thus, the calcination temperature of 400°C is favourable for the fabrication of V_2O_5 nanomaterials with belt-like shape. Keeping other parameters constant, only the calcination time was considered as the changeable parameter. The synthesis experiments were carried out at definite calcination periods of 1, 2, 4 and 12 h, EtOH/H_2O= 10/25 and calcination temperature = 400°C. XRD patterns (figure 8a) revealed that pure-phase V_2O_5 was synthesized over 1–12 h,

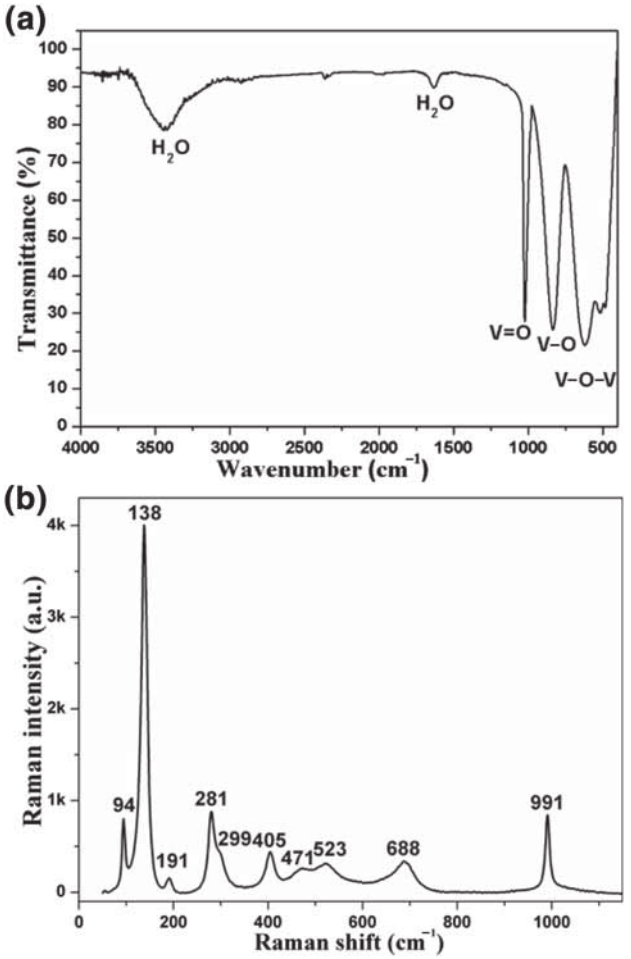

Figure 4. (**a**) IR spectrum and (**b**) Raman spectrum of the as-obtained V_2O_5.

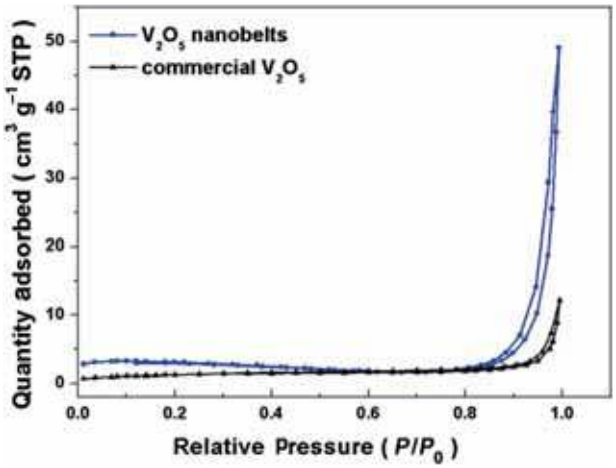

Figure 5. Nitrogen adsorption–desorption isotherms of the as-obtained V_2O_5 and the commercial V_2O_5.

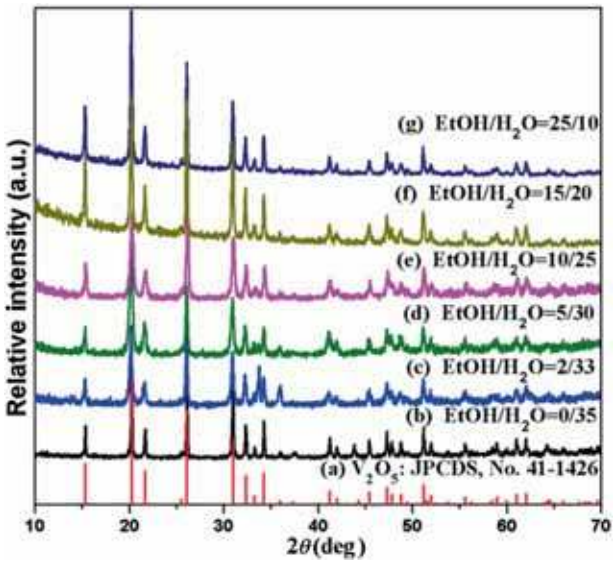

Figure 6. XRD patterns of the as-obtained samples obtained at various volume ratios of EtOH/H_2O and calcination at 400°C for 4 h.

and FE-SEM images shown in figure 9a (1 h) and b (12 h) reveal that V_2O_5 nanomaterials were obtained. These results indicate that the calcination time has little influence on the composition and morphology of the products in this range.

3.3 *Electrochemical properties*

To exhibit the merits of the as-obtained V_2O_5 nanomaterials, the electrochemical investigation of the pseudocapacitance was evaluated by CV and GCD methods in a three-electrode cell. Figure 10 shows the CV curves of V_2O_5 nanomaterials with various potential limits, which reveal that the potential limit from −0.5 to 0.6 V shows a good symmetry and high capacity. Thus, the CV and GCD tests of V_2O_5 nanomaterials were recorded in the potential range −0.5 to 0.6 V.

Figure 11 displays the CV curves of V_2O_5 nanomaterials recorded at different scan rates from 5 to 100 mV s^{-1} within a potential window of −0.5 to 0.6 V in 1 mol l^{-1} $LiNO_3$ electrolyte. Each CV curve shows two pairs of redox peaks (two anodic peaks at positive current density and two cathodic peaks at negative current density), which indicate superior faradaic reactions at the electrode surface and the electrochemical redox reaction based on the Li ion intercalation and extraction is associated with the equation as follows [56]:

$$V_2O_5 + xLi + xe^- \underset{\text{charge}}{\overset{\text{discharge}}{\rightleftharpoons}} Li_xV_2O_5\ (0 \le x \le 1).$$

Changes of crystal phases occurred along with the entire process, which were generally designated as α ($0 < x < 0.1$), ε ($0.35 < x < 0.5$) and δ ($0.9 < x < 1$) [17,56]. As shown in figure 11, the shape of the CV curves mainly does not change at different scan rates, which indicates an excellent pseudo-capacitive response of the electrode material. The response current of the electrode increases with the increase

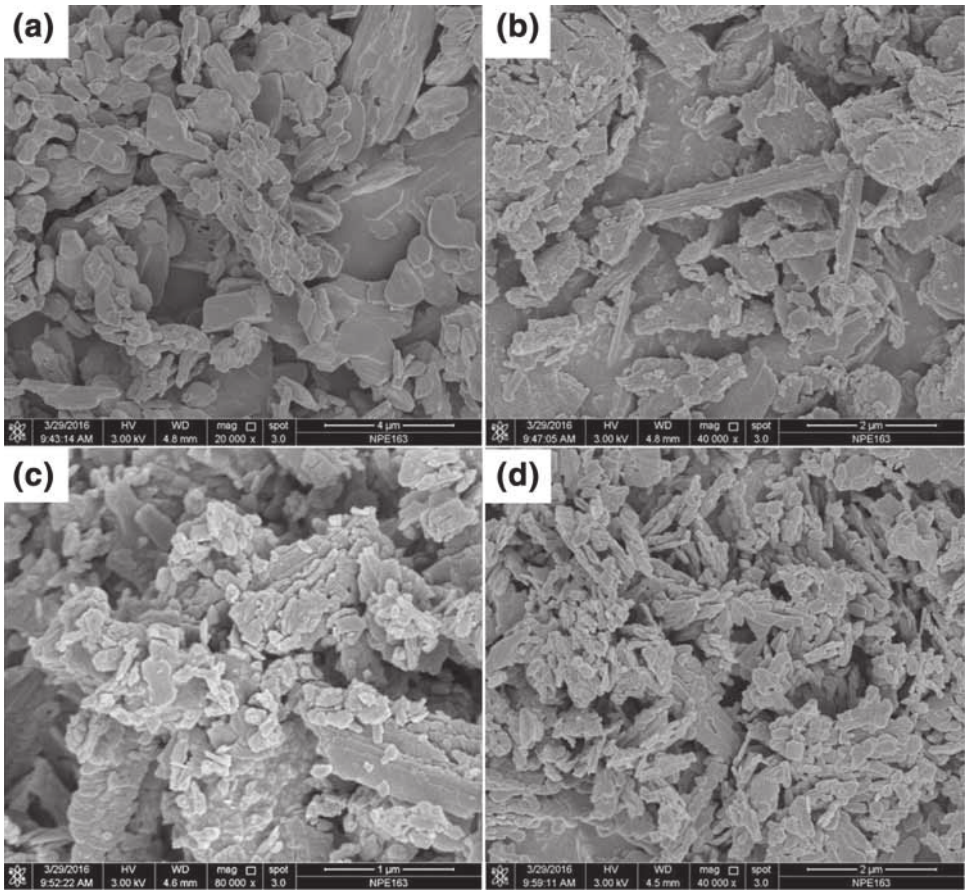

Figure 7. FE-SEM images of the as-obtained samples obtained at various volume ratios of EtOH/H_2O and calcination at 400°C for 4 h: (**a**) 0/35, (**b**) 2/33, (**c**) 5/30 and (**d**) 25/10.

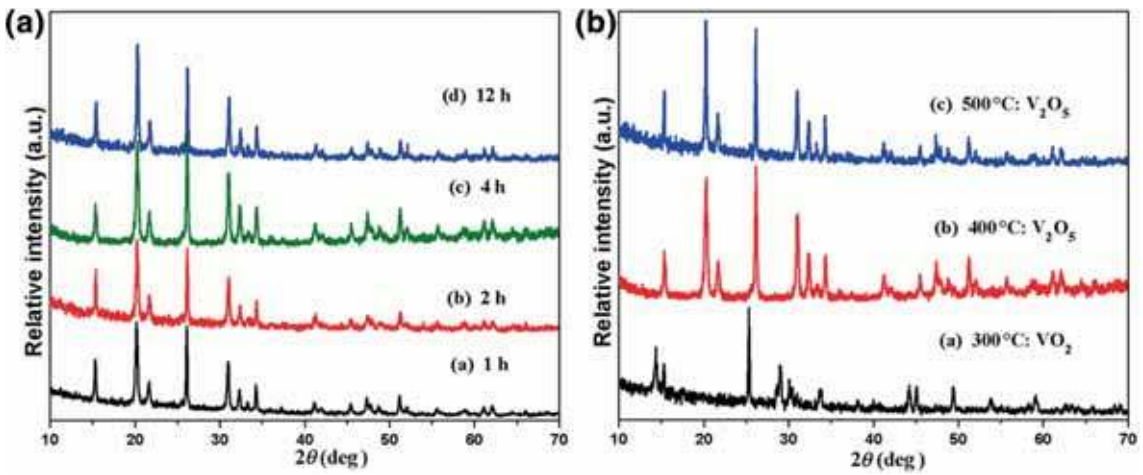

Figure 8. XRD patterns of the as-obtained samples obtained at volume ratio of EtOH/H_2O = 10/25 and various calcination times and temperatures.

in scan rate, which demonstrates the excellent kinetics and reversibility of the electrode [11,32]. Furthermore, the oxidation peaks shift positively and reduction peaks shift negatively with the increasing of scan rates, which is attributed to the polarization effect of the electrode [11,32]. The separation between the two redox peaks increased significantly with the scan rate increasing from 5 to 100 mV s^{-1}, which is due to the increase of overpotentials [17]. As shown in figure 11, the

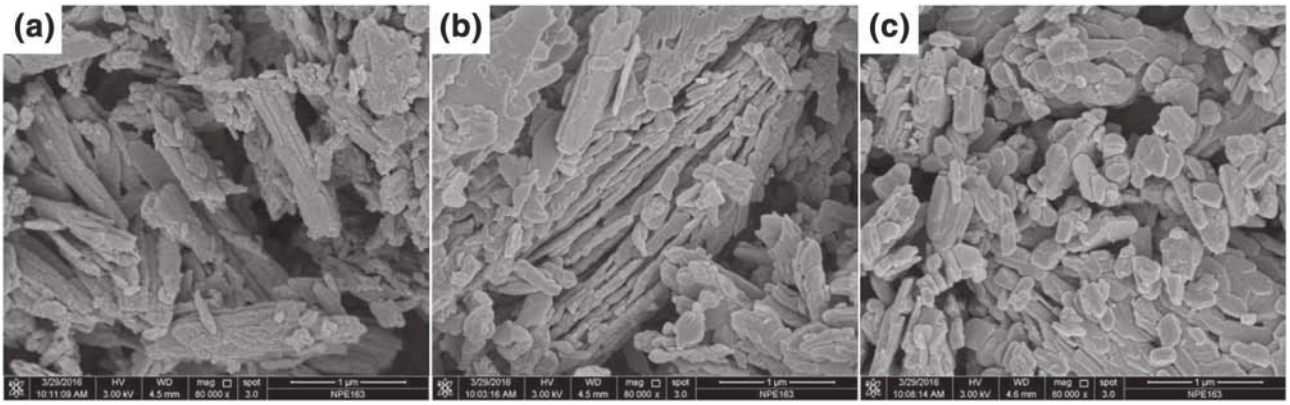

Figure 9. FE-SEM images of the as-obtained samples obtained at volume ratio of EtOH/H_2O = 10/25 and various calcination times and temperatures: (**a**) 1 h, (**b**) 12 h and (**c**) 500°C.

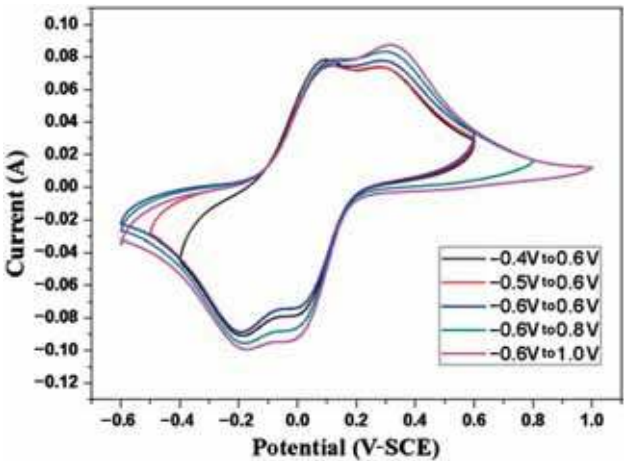

Figure 10. CV curves of V_2O_5 nanobelts over various potential limits.

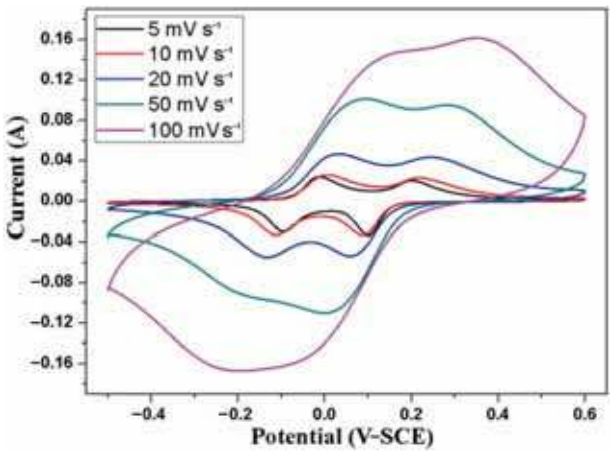

Figure 11. CV curves of V_2O_5 nanomaterials at different scan rates.

redox peaks still exist even at 100 mV s^{-1}, which indicates that this material has good rate capability [38].

To reveal the influence of the synthesis conditions on the electrochemical properties of various samples, their corresponding CV and GCD tests were performed and are shown in supplementary figure S2 and figure 12. Supplementary figure S2a shows the CV curves of the samples obtained with different volume ratios of EtOH/H_2O = 0/35, 2/33, 5/30, 10/25, 15/20, 25/10 and calcination at 400°C for 4 h. All the curves have similar shapes and exhibit two pairs of redox peaks, indicating that all samples have pseudocapacitive behaviour and the values of pseudocapacitance are given by GCD. Figure 12a shows their corresponding variation of potential *vs.* time for charge–discharge cycle recorded on GCD test at a high current density of 1 A g^{-1}. The relatively symmetrical potential–time curves can be observed. Each curve has two distinct potential plateaus, which is consistent with the redox peaks in CV curves depicted in supplementary figure S2a. This indicates that the high value is mainly caused by faradic pseudocapacitance, which is much higher than the double-layer capacitance. The peak in high potential illustrates that the capacitive behaviour is influenced by electrical double-layer structure accompanied by the redox reaction, which arises from the electrochemical adsorption and release at the interface of the electrode and electrolyte [32]. From figure 12, it is clearly observed that V_2O_5 synthesized at EtOH/H_2O = 10/25 displays the highest specific capacitance. The specific capacitance of V_2O_5 prepared at EtOH/H_2O = 0/35, 2/33, 5/30, 10/25, 15/20 and 25/10 are, respectively, 289, 319, 376, 406, 353 and 335 F g^{-1}. These results indicate that V_2O_5 nanomaterials with rough surface (EtOH/H_2O = 10/25) exhibit an excellent energy storage capability. The reason may be due to the structure of the as-obtained V_2O_5 nanomaterials with rough surface having large specific surface area (figures 2, 3 and 5) [31,57].

Supplementary figure S2b and figure 12b, respectively, show the CV curves and potential *vs.* time for charge–discharge cycle curves of the samples obtained at the volume ratio of EtOH/H_2O = 10/25 and calcination at 300, 400 and

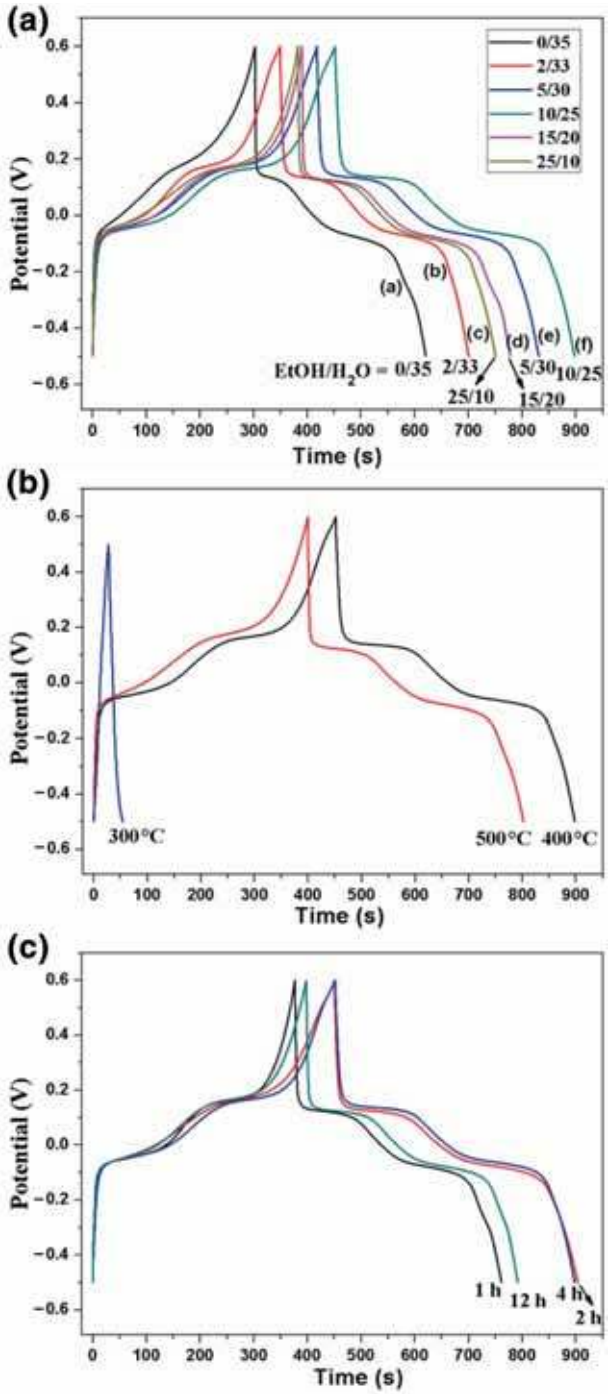

Figure 12. Potential *vs.* time for charge and discharge profiles of the samples obtained at various conditions at a current density of 1 A g^{-1}.

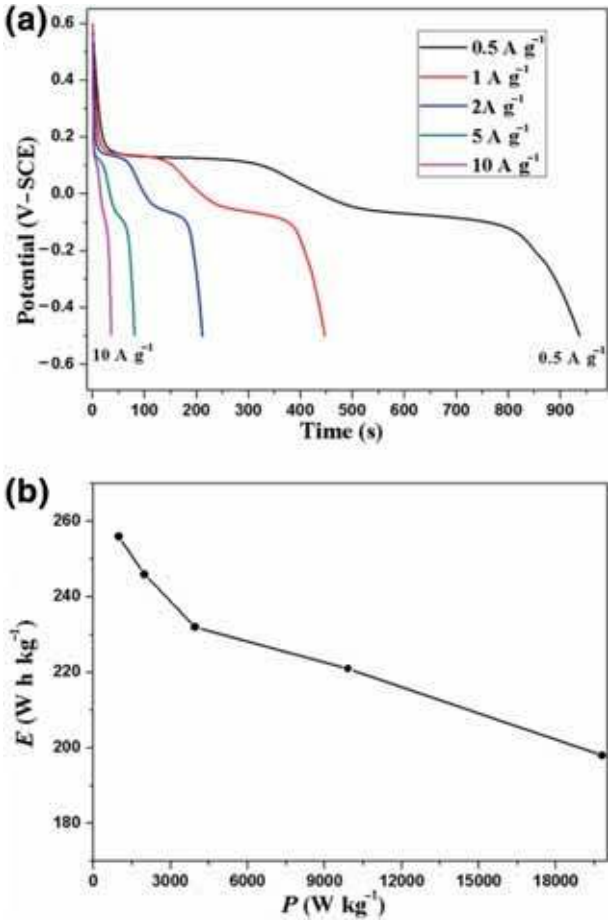

Figure 13. (**a**) Galvanostatic discharge curves at different current densities of V_2O_5 nanomaterials. (**b**) Ragone plot of V_2O_5 nanomaterials.

500°C for 4 h. There is no redox peak in CV curve of the sample synthesized at 300°C, suggesting that it possesses only the double-layer capacitance. Its capacitance is very low, only 25 F g^{-1} (figure 12b), because VO_2 is prepared at 300°C (figure 8) and its pseudocapacitive behaviour is not displayed in the potential limit over −0.5 to 0.6 V [58]. When the calcination temperature is increased to 500°C, a similar CV curve is obtained as that at 400°C, and its capacitance is 376 F g^{-1} (figure 12b). The capacitance is lower than that of V_2O_5 nanomaterials (400°C) owing to irregular morphology obtained at higher temperature (figure 9c). Supplementary figure S2c and figure 12c, respectively, show the CV curves and potential *vs.* time for charge–discharge cycle curves of the samples obtained at the volume ratio of $EtOH/H_2O = 10/25$ and calcination at 400°C for 1, 2, 4 and 12 h. All the curves have similar shapes, indicating that all samples have pseudocapacitive behaviour. The specific capacitances of V_2O_5 prepared for the calcination times of 1, 2, 4 and 12 h are, respectively, 350, 410, 405 and 358 F g^{-1}. Based on these results, V_2O_5 nanomaterials synthesized at $EtOH/H_2O = 10/25$ and calcination at 400°C for 2–4 h exhibit the best electrochemical property.

V_2O_5 nanomaterials with rough surface have the best electrochemical property of all the samples; thus, we used these materials to investigate their rate capability and cycling performance. Figure 13 shows the discharge curves obtained at various current densities. According to equation (1), the specific capacitance of the V_2O_5 nanomaterials calculated from the discharge time is 423, 405, 383, 365 and 327 F g^{-1} at

Table 1. Comparison of specific capacitance of V_2O_5 nanomaterials with rough surface with V_2O_5 materials reported in the previous literatures.

Types of V_2O_5 material	Electrolyte	Potential range (V)	Specific capacitance (F g^{-1})	Reference
$V_2O_5 \cdot 0.6H_2O$ nanoribbons	0.5 mol l^{-1} K_2SO_4	0–1	181	[39]
V_2O_5 nanoflowers, nanoballs, nanowires, nanorods	1 mol l^{-1} Na_2SO_4	0–1	119, 161, 177, 235	[32]
V_2O_5 nanobelts, nanoparticles, microspheres	1 mol l^{-1} $LiNO_3$	−0.4 to 0.8	140, 276, 308	[11]
Electrospun V_2O_5 nanofibres	2 mol l^{-1} KCl	0–0.9 V	190	[15]
Electrospun V_2O_5 nanofibres	1 mol l^{-1} $LiClO_4$ in PC	0–3	250	[15]
Nanoporous V_2O_5	2 mol l^{-1} KCl	−0.2 to 0.8	214	[41]
V_2O_5 powders	2 mol l^{-1} KCl	−0.2 to 0.7	262	[13]
Interconnected V_2O_5 nanoporous network	0.5 mo l l^{-1} K_2SO_4	0.2–0.8 V	304	[34]
V_2O_5 nanowires	1 mol l^{-1} $LiNO_3$	−0.4 to 0.8	351	[38]
Hollow spherical V_2O_5	5 mol l^{-1} $LiNO_3$	−0.2 to 0.8	479	[17]
β-V_2O_5 thin films	1 mol l^{-1} $LiClO_4$ in PC	−0.8 to 1.2	346	[37]
V_2O_5 nanomaterials with rough surface	1 mol l^{-1} $LiNO_3$	−0.5 to 0.6	423	This work

the current density of 0.5, 1, 2, 5 and 10 A g^{-1}, respectively. If the current is higher, the specific capacity is much lower. The specific capacitance gradually decreases at higher current densities owing to the incremental voltage drop and insufficient active material being involved in the redox reaction at a higher current density [59]. Besides, the process of charge–discharge at a high current density may lead to a low utilization rate of active material [1]. The attenuation of specific capacitance slowly reduces from low current density to high current density (0.5–10 A g^{-1}). About 77% of the capacitance value (at a current density of 10 A g^{-1}) can remain compared with that at a current density of 0.5 A g^{-1}. This good rate capability is attributed to the novel structure of V_2O_5 nanomaterials. The specific capacitance of the as-obtained V_2O_5 nanomaterials with rough surface outperforms that of other V_2O_5 materials, as summarized in table 1. It can be seen that V_2O_5 nanomaterials with rough surface have better electrochemical properties than most references. However, the specific capacitance of V_2O_5 nanomaterials with rough surface is slightly lower than that of hollow V_2O_5 microspheres and the reason is that the specific surface area of V_2O_5 materials in this work is bigger than our present work. Besides, the electrochemical properties of V_2O_5 nanomaterials are lower than those of copper-foam-integrated three-dimensional graphene networks [60]. Figure 13b shows a Ragone plot of the as-prepared V_2O_5 nanomaterials. According to equations (2) and (3), the calculated E at the current density of 0.5, 1, 2, 5 and 10 A g^{-1} is 256, 246, 232, 221 and 198 W h kg^{-1}, respectively, and the corresponding P is 984, 1985, 3962, 9908 and 19,800 W kg^{-1}, respectively, which exhibits the outstanding electrochemical performance of V_2O_5 nanomaterials. Therefore, nano-structured V_2O_5 prepared in this work using a simple chemical route exhibits an excellent capacity

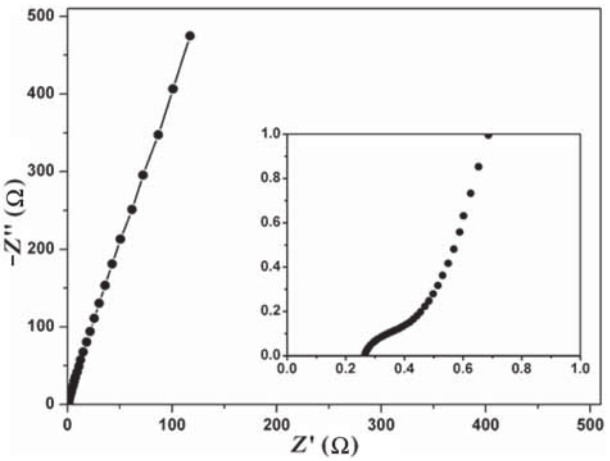

Figure 14. The electrochemical impedance spectroscopy of V_2O_5 nanomaterials obtained over the frequency range of 100 kHz to 0.01 Hz.

compared with other literature reports. To disclose the reason of V_2O_5 nanomaterials with rough surface exhibiting the best electrochemical behaviour, EIS was carried out over a frequency range of 100 kHz to 0.01 Hz, as shown in figure 14. The EIS data are modelled via the well-known $R-C$ equivalent circuit [61]. It is clearly observed that the semicircle diameter of V_2O_5 nanomaterials is very small, which indicates the high electric conductivity of V_2O_5 nanomaterials with rough surface.

Furthermore, the cycling performance of V_2O_5 nanomaterials was also evaluated by CV and GCD tests, as shown in figures 15, supplementary figures S3 and S4. Figures 15a and supplementary figure S3 show the cycling behaviour

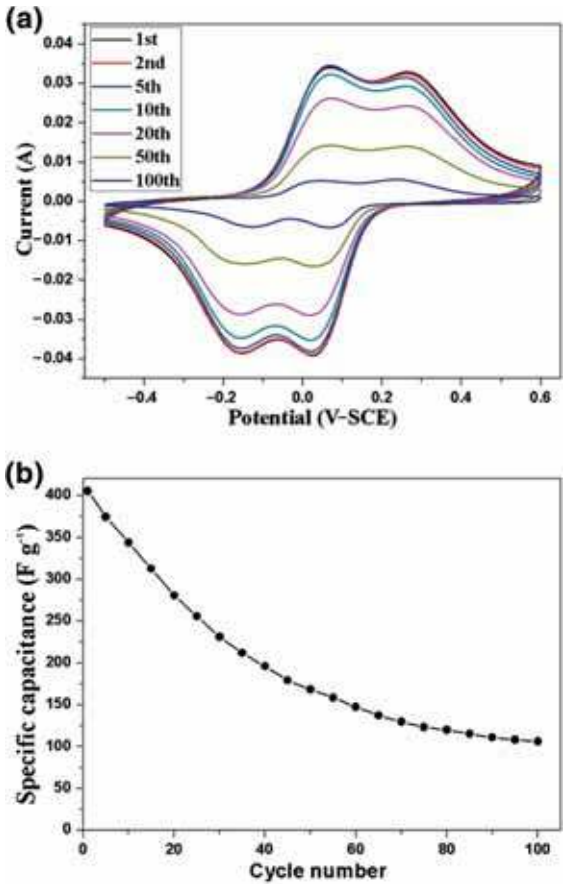

Figure 15. (**a**) Cycling behaviour of the V_2O_5 nanomaterials recorded at a current density of 1 A g^{-1} by CV and (**b**) the cyclic stability of the specific capacitance of the V_2O_5 nanomaterials by GCD.

of V_2O_5 nanomaterials electrodes recorded by CV at 20 mV s^{-1} scan rate, which intuitively reveal that the specific capacitance quickly fades with the increasing cycles. Supplementary figure S4 reveals the GCD profiles at a current density of 1 A g^{-1}. Figure 15b, obtained from supplementary figure S4, exhibits the change of the specific capacitance. The specific capacitances of V_2O_5 nanomaterials are 344, 196 and 106 F g^{-1} after 10, 40 and 100 cycles, respectively. Their corresponding retentions after 10, 40 and 100 cycles are 85, 48 and 26% of the initial discharge capacity. Furthermore, the cycling performance of V_2O_5 nanomaterials was further evaluated by GCD at a current density of 0.5 A g^{-1}, as shown in supplementary figure S5. The specific capacitances of V_2O_5 nanomaterials are 350, 185 and 78 F g^{-1} after 10, 40 and 100 cycles, respectively. Their corresponding retentions after 10, 40 and 100 cycles are 82, 44 and 18% of the initial discharge capacity. These results show that the specific capacitance quickly fades with the increasing cycles. The reason may be related with phase conversion and dissolution of the V_2O_5 material. As shown in figure 15a, the redox peaks in all the cycles can be obviously detected in the CV curves. Supplementary figure S4 displays the characteristic plateaus, which exist at almost identical potentials during the whole cycling process in the GCD result. These results indicate that the phase transition is completely reversible with increasing numbers of cycles. Hence, phase transformation of the V_2O_5 material cannot be the reason for the fast fading of the specific capacitance. The dissolution of electrode material in aqueous $LiNO_3$ solution might be a reason because the electrolyte solution gradually turns yellow (the colour of V_2O_5 solution) during the constant charge–discharge process, which is a common phenomenon for vanadium oxides used as electrodes for supercapacitors and Li-ion batteries [44,62]. Moreover, the strong stress introduced by the structure expansion during Li-ion insertion into the V_2O_5 easily caused the structure to collapse, which promotes dissolution [38]. This explanation can be also proved by the evidence provided by FE-SEM observation. Figure 16 shows the SEM images of the

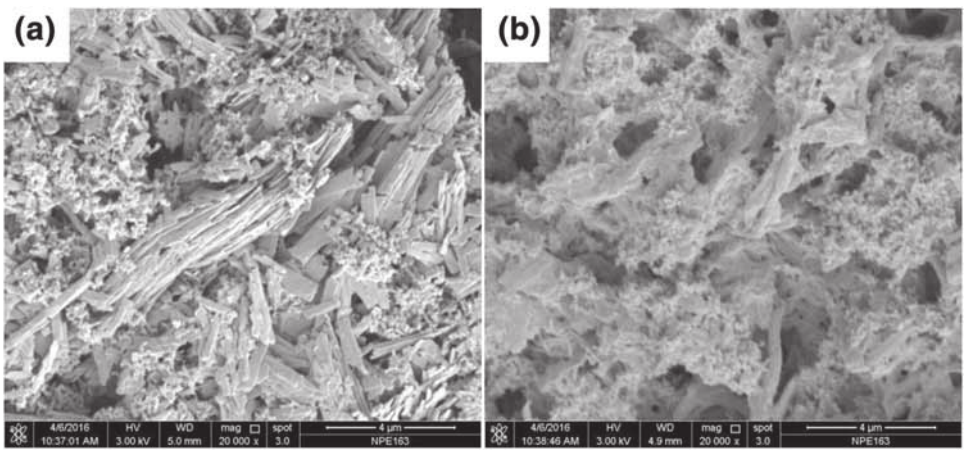

Figure 16. FE-SEM images of the working V_2O_5 nanomaterials electrodes (**a**) before and (**b**) after the cycles.

working electrodes before and after the cycles, which clearly show that the working V_2O_5 materials are much less after the cycles and the structure of V_2O_5 materials collapses (figure 16b).

4. Conclusion

In summary, V_2O_5 nanomaterials with rough surface were synthesized using commercial V_2O_5, ethanol (EtOH) and H_2O as the starting materials by a simple hydrothermal route and combined with a post-annealing process. The composition, morphology and structure of the samples were characterized by XRD, IR, BET, FE-SEM and TEM. The electrochemical properties of V_2O_5 nanomaterials reveal that they exhibit a tremendous pseudocapacitance effect when used as electrodes for supercapacitors. V_2O_5 nanomaterials exhibit the specific capacitance of 423 F g^{-1} at the current density of 0.5 A g^{-1} and retain 327 F g^{-1} even at high current density of 10 A g^{-1}. The influences of the ratio of EtOH/H_2O, the calcination time and temperature on the morphology, purity and electrochemical property of the products were discussed in detail. The results revealed that the ratio of EtOH/H_2O = 10/25 and calcination at 400°C for 2–4 h are favourable for preparing V_2O_5 nanomaterials and they exhibited the best electrochemical property. The novel morphology and high specific surface area are the main factors that contribute to higher electrochemical performance to V_2O_5 nanomaterials during the charge–discharge processes. The specific capacitance of V_2O_5 nanomaterials electrodes faded with the increasing cycles, and the reason is the dissolution of electrode material in aqueous $LiNO_3$ solution. The significance of this work is that it provides more insights about the effect of structures on the electrochemical properties of vanadium oxides with novel structures.

Acknowledgements

This work was partially supported by the National Natural Science Foundation of China (Grant No. 21601026), Fundamental Research Funds for the Central Universities (DUT16LK37), Doctoral Research Foundation of Liaoning Province (201601035) and Science Research Project of Liaoning Province Education Department (L2015123).

References

[1] Yu Z, Tetard L, Zhai L and Thomas J 2015 *Energ. Environ. Sci.* **8** 702
[2] Cao L, Zhu J, Li Y, Xiao P, Zhang Y, Zhang S *et al* 2014 *J. Mater. Chem. A* **2** 13136
[3] Zhang Y and Meng C 2016 *J. Alloys Compd.* **674** 259
[4] Winter M and Brodd R J 2004 *Chem. Rev.* **104** 4245
[5] Zhang Y, Fan M, Zhou M, Huang C, Chen C, Cao Y *et al* 2012 *Bull. Mater. Sci.* **35** 369
[6] Rui X, Tang Y, Malyi O I, Gusak A, Zhang Y, Niu Z *et al* 2016 *Nano Energy* **22** 583
[7] Zhang Y and Meng C 2015 *Mater. Lett.* **160** 404
[8] Zhang Y and Huang Y 2016 *Mater. Lett.* **182** 285
[9] Zhou X, Chen Q, Wang A, Xu J, Wu S and Shen J 2016 *ACS Appl. Mater. Interfaces* **8** 3776
[10] Lee M, Balasingam S K, Jeong H Y, Hong W G, Lee H-B-R, Kim B H *et al* 2015 *Sci. Rep.* **5** 8151
[11] Zhang Y, Zheng J, Zhao Y, Hu T, Gao Z and Meng C 2016 *Appl. Surf. Sci.* **377** 385
[12] Zhang L L and Zhao X S 2009 *Chem. Soc. Rev.* **38** 2520
[13] Lao Z J, Konstantinov K, Tournaire Y, Ng S H, Wang G X and Liu H K 2006 *J. Power Sources* **162** 1451
[14] Yang D 2013 *J. Power Sources* **228** 89
[15] Wee G, Soh H Z, Cheah Y L, Mhaisalkar S G and Srinivasan M 2010 *J. Mater. Chem.* **20** 6720
[16] Xia X, Zhang Y, Chao D, Guan C, Zhang Y, Li L *et al* 2014 *Nanoscale* **6** 5008
[17] Yang J, Lan T, Liu J, Song Y and Wei M 2013 *Electrochim. Acta* **105** 489
[18] Qian T, Xu N, Zhou J, Yang T, Liu X, Shen X *et al* 2015 *J. Mater. Chem. A* **3** 488
[19] Wu Y, Gao G and Wu G 2015 *J. Mater. Chem. A* **3** 1828
[20] Wu Y, Gao G, Yang H, Bi W, Liang X, Zhang Y *et al* 2015 *J. Mater. Chem. A* **3** 15692
[21] Zhang Y, Chen C, Wu W, Niu F, Liu X, Zhong Y *et al* 2013 *Ceram. Int.* **39** 129
[22] Zhang Y, Zhou M, Fan M, Huang C, Chen C, Cao Y *et al* 2011 *Curr. Appl. Phys.* **11** 1159
[23] Zhang Y, Fan M, Liu X, Huang C and Li H 2012 *Eur. J. Inorg. Chem.* **2012** 1650
[24] Rauda I E, Augustyn V, Saldarriaga-Lopez L C, Chen X, Schelhas L T, Rubloff G W *et al* 2014 *Adv. Funct. Mater.* **24** 6717
[25] Zhang Y, Wang N, Huang Y, Wu W, Huang C and Meng C 2014 *Ceram. Int.* **40** 11393
[26] Zhang Y, Zhang J, Zhang X, Deng Y, Zhong Y, Huang C *et al* 2013 *Ceram. Int.* **39** 8363
[27] Zhang Y, Zhang J, Fan M, Long Y A, Zhong Y, Liu X *et al* 2013 *Bull. Mater. Sci.* **36** 345
[28] Xu L, Zhang Y, Zhang X, Huang Y, Tan X, Huang C *et al* 2014 *Bull. Mater. Sci.* **37** 1397
[29] Zhang Y, Zhang J, Zhang X, Mo S, Wu W, Niu F *et al* 2013 *J. Alloys Compd.* **570** 104
[30] Zhang Y, Li W, Fan M, Zhang F, Zhang J, Liu X *et al* 2012 *J. Alloys Compd.* **544** 30
[31] Zhu J, Cao L, Wu Y, Gong Y, Liu Z, Hoster H E *et al* 2013 *Nano Lett.* **13** 5408
[32] Mu J, Wang J, Hao J, Cao P, Zhao S, Zeng W *et al* 2015 *Ceram. Int.* **41** 12626
[33] Kim B-H, Kim C H, Yang K S, Rahy A and Yang D J 2012 *Electrochim. Acta* **83** 335
[34] Saravanakumar B, Purushothaman K K and Muralidharan G 2012 *ACS Appl. Mater. Interfaces* **4** 4484
[35] Peng T, Wang J, Liu Q, Liu J and Wang P 2015 *CrystEngComm.* **17** 1673
[36] Zheng J, Zhang Y, Jing X, Wang Q, Hu T, Xing N *et al* 2017 *Mater. Chem. Phys.* **166** 5
[37] Jeyalakshmi K, Vijayakumar S, Nagamuthu S and Muralidharan G 2013 *Mater. Res. Bull.* **48** 760

[38] Wang N, Zhang Y, Hu T, Zhao Y and Meng C 2015 *Curr. Appl. Phys.* **15** 493
[39] Qu Q T, Shi Y, Li L L, Guo W L, Wu Y P, Zhang H P *et al* 2009 *Electrochem. Commun.* **11** 1325
[40] Yu M, Liu X, Wang Y, Zheng Y, Zhang J, Li M *et al* 2012 *Appl. Surf. Sci.* **258** 9554
[41] Reddy R N and Reddy R G 2006 *J. Power Sources* **156** 700
[42] Guo Y, Li J, Chen M and Gao G 2014 *J. Power Sources* **273** 804
[43] Yilmaz G, Guo C X and Lu X 2016 *ChemElectroChem.* **3** 158
[44] Li H-Y, Wei C, Wang L, Zuo Q-S, Li X, Xie B 2015 *J. Mater. Chem. A* **3** 22892
[45] Saravanakumar B, Purushothaman K K and Muralidharan G 2015 *J. Electroanal. Chem.* **758** 111
[46] Gilson T R, Bizri O F and Cheetham N 1973 *J. Chem. Soc. Dalton Trans.* **3** 291
[47] Chen W, Mai L, Peng J, Xu Q and Zhu Q 2004 *J. Mater. Sci.* **39** 2625
[48] Baddour-Hadjean R, Smirnov M B, Smirnov K S, Kazimirov V Y, Gallardo-Amores J M, Amador U *et al* 2012 *Inorg. Chem.* **51** 3194
[49] Baddour-Hadjean R, Marzouk A and Pereira-Ramos J P 2012 *J. Raman Spectrosc.* **43** 153
[50] Zhang Y, Zheng J, Wang Q, Hu T, Tian F and Meng C 2017 *Appl. Surf. Sci.* **399** 151
[51] Horrocks G A, Likely M F, Velazquez J M and Banerjee S 2013 *J. Mater. Chem. A* **1** 15265
[52] Faggio G, Modafferi V, Panzera G, Alfieri D and Santangelo S 2012 *J. Raman Spectrosc.* **43** 761
[53] Baddour-Hadjean R, Golabkan V, Pereira-Ramos J P, Mantoux A and Lincot D 2002 *J. Raman Spectrosc.* **33** 631
[54] Zhang Y, Liu X, Xie G, Yu L, Yi S, Hu M 2010 *Mater. Sci. Eng. B* **175** 164
[55] Li H Q, Zhai T Y, He P, Wang Y G, Hosono E and Zhou H S 2011 *J. Mater. Chem.* **21** 1780
[56] Delmas C, Cognac-Auradou H, Cocciantelli J M, Menetrier M and Doumerc J P 1994 *Solid State Ion.* **69** 257
[57] Zhou H S, Li H Q, He P, Wang Y G and Hosono E 2011 *J. Mater. Chem.* **21** 10999
[58] Zhang Y, Zheng J, Hu T, Tian F and Meng C 2016 *Appl. Surf. Sci.* **371** 189
[59] Deng L, Zhang G, Kang L, Lei Z, Liu C and Liu Z-H 2013 *Electrochim. Acta* **112** 448
[60] Dey R S, Hjuler H A and Chi Q 2015 *J. Mater. Chem. A* **3** 6324
[61] Li H-Y, Jiao K, Wang L, Wei C, Li X and Xie B 2014 *J. Mater. Chem. A* **2** 18806
[62] Zhang Y, Zheng J, Wang Q, Hu T and Meng C 2016 *RSC Adv.* **6** 93741